frontiers | Frontiers in Materials

TYPE Original Research
PUBLISHED 08 June 2023
DOI 10.3389/fmats.2023.1198776

OPEN ACCESS

EDITED BY
Ehsan Ghasali,
Materials and Energy Research Center, Iran

REVIEWED BY
Wenbin Zhou,
University of Dundee, United Kingdom
Yingyi Zhang,
Anhui University of Technology, China

*CORRESPONDENCE
Miaohui Wang,
wangmh0103@163.com
Zhen Si,
sizhen0702@163.com
Dongyue Zhang,
814798860@qq.com

RECEIVED 02 April 2023
ACCEPTED 01 June 2023
PUBLISHED 08 June 2023

CITATION
Hu Q, Wang M, Chen Y, Si Z and Zhang D (2023), Effects of sintering temperatures on the microstructure and mechanical properties of S390 powder metallurgy high-speed steel.
Front. Mater. 10:1198776.
doi: 10.3389/fmats.2023.1198776

Effects of sintering temperatures on the microstructure and mechanical properties of S390 powder metallurgy high-speed steel

Qipeng Hu[1,2,3], Miaohui Wang[1,2,3]*, Yunbo Chen[1,2], Zhen Si[1]* and Dongyue Zhang[2,3]*

[1]China Academy of Machinery Science and Technology Group Co., Ltd., Beijing, China, [2]Beijing National Innovation Institute of Lightweight Co., Ltd., Beijing, China, [3]China Machinery Institute of Advanced Materials Co., Ltd., Zhengzhou, China

High-performance complex gear cutters and high-temperature bearings are just some of the applications where high-speed steels (HSSs) shine as a preferred material choice owing to their high hardness and outstanding wear resistance. In this work, the effects of sintering temperature on the microstructure and mechanical properties of S390 HSS prepared via spark plasma sintering (SPS) were investigated with a range of sintering temperatures from 930°C to 1,090°C, a uniaxial pressure of 50 MPa, and a holding time of 5 min. The results demonstrated that the improvements in density, hardness, red hardness, and three-point bending strength were confirmed as the sintering temperature increased from 930°C to 1,090°C. Temperature-induced microstructure evolutions were assessed for their contribution to property enhancement, such as powders with varying dimensions and carbides with diverse morphology and diameter. The specimen with the best comprehensive mechanical properties (67.1 HRC and 1,196.67 MPa) was prepared at 1,050°C via SPS. The wear coefficients decreased as the sintering temperature increased, and the observation results of worn surfaces of test pins confirmed that abrasive wear and oxidation wear dominated the wear experiments. Furthermore, the wear mechanism of dense and porous SPS HSS was illustrated and analyzed in terms of the debris and trapped carbides.

KEYWORDS

high-speed steel, sintering temperature, hardness, abrasive wear, microstructure

1 Introduction

Given its outstanding hardness and wear resistance throughout the working process, high-speed steel (HSS) is an essential industrial material for the production of sophisticated cutting tools and high-temperature bearings (Xiang et al., 2020; Zhang et al., 2021; Furuya et al., 2022; Wang et al., 2022; Xu et al., 2022). One of the advantages of HSS over hard metals and ceramic materials is its ability to achieve the complicated shapes with the necessary and desirable bending strength. As technology and industry advance, the application of powder metallurgy (PM) technology in manufacturing HSS has refined the size and distribution of carbides, which has also allowed for the production of PMHSS with a higher alloy content. The powder metallurgy process has the potential to eliminate the segregation of carbides, and

the different consolidation techniques might be doing this, such as hot isostatic pressing (HIP) (Benito et al., 2021; Yang et al., 2021), spark plasma sintering (SPS) (Hu et al., 2022; Madej et al., 2022), and metal injection molding (MIM) (Herranz et al., 2017; Mukund and Hausnerova, 2020). In contrast to other PM processes, the SPS technique, in which temperature and uniaxial pressure are simultaneously applied to the powder, has the advantages of a short sintering time and a low sintering temperature, and the Joule heating effect and electric field effect caused by pulsed direct current accelerate the consolidation process (Zhang et al., 2017; Shen et al., 2019; Zeng et al., 2019; Shen et al., 2020).

Controlling the microstructure and mechanical characteristics of PMHSS is dependent on the sintering and heat treatment parameters, such as pressure and temperature (Leskovšek and Podgornik, 2012; Peng et al., 2018a; Peng et al., 2018b; Yan et al., 2022). During the sintering process, temperature plays a crucial role in densification; a suitable temperature might not only achieve the aim of obtaining a specimen with almost full density but also prevent the formation of the liquid phase in order to limit carbide precipitation and growth. When sintering temperatures rose and particle size decreased within a particular range, the density of as-sintered specimens approached that of full density (Matteazzi and Wolf, 1998). Excessive sintering temperatures stimulate the production of massive carbides at the prior powder boundary, which weakens the impact toughness (Romero et al., 2020; Li et al., 2023). Moreover, the absence and composition of the atmosphere have an impact on the PM specimens, particularly their microstructure and characteristics (Asgharzadeh and Simchi, 2005; Shashanka and Chaira, 2016). An extra attention should be focused on the holding time of SPS process, numerous studies have shown that proper extension of the sintering holding time could improve the densities and properties of the specimens (Park et al., 2011; Yamanoglu et al., 2013; Oke et al., 2018; Wang et al., 2021; Hasan et al., 2023). However, prolonged high temperature heat treatment of HSS might lead to the growth of carbides and grains, and the low lifetime of graphite dies.

The impact of heat treatment on the mechanical characteristics of HSS has been the subject of many investigations. The influence of sintering temperature on properties and microstructure, with respect to the less dense PMHSS in particular, has been the subject of a few small academic studies. Mechanical properties and microstructure in PMHSS have not been shown to be affected by SPS sintering temperature.

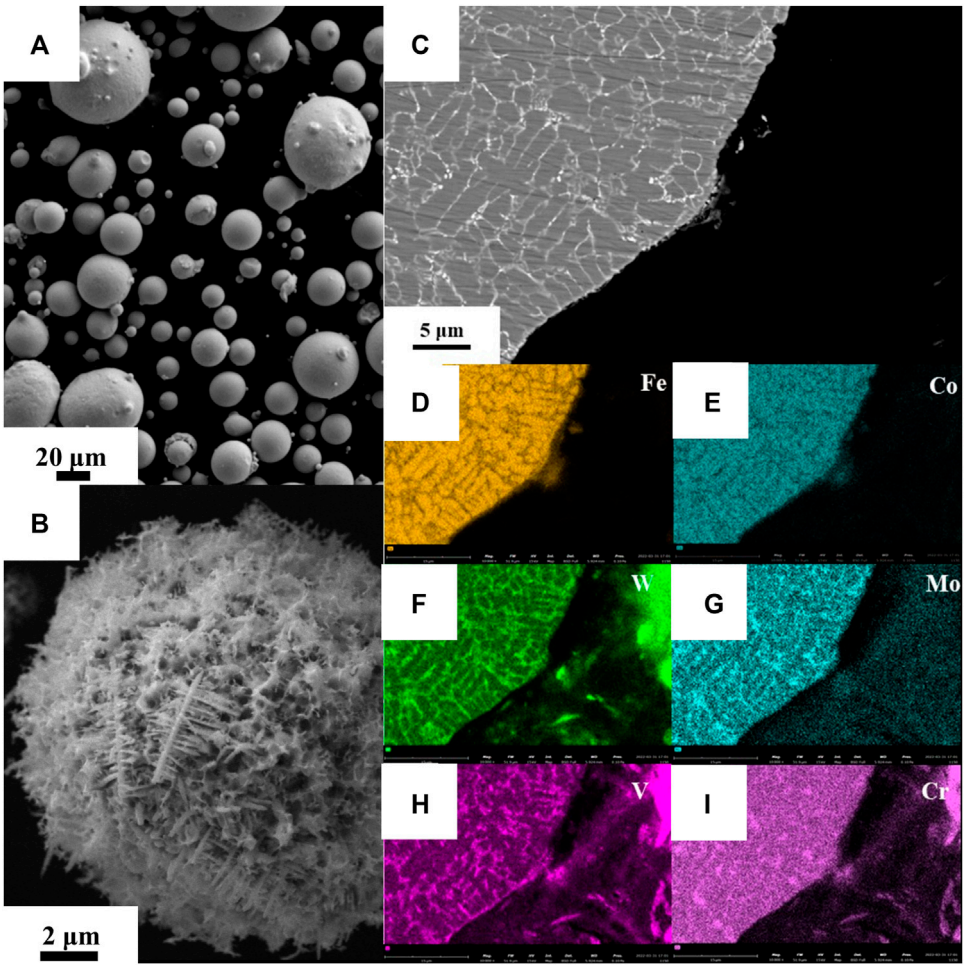

FIGURE 1
Characterizations of S390 HSS powders:**(A)** Morphology; **(B)** Carbide dendrites; **(C)** Cross section microstructure; **(D–I)** EDS results.

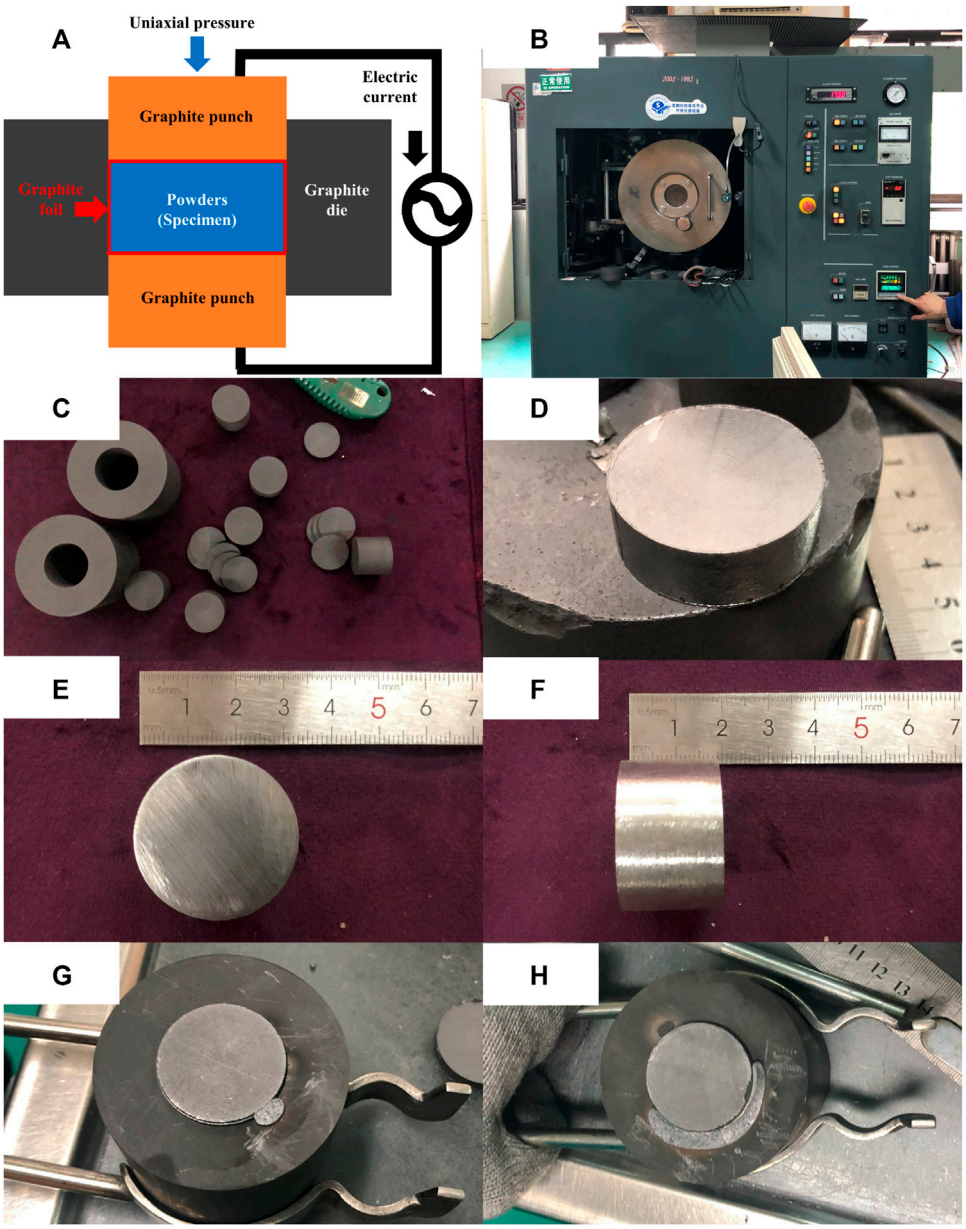

FIGURE 2
Schematic diagram and physical photos of SPS: **(A)** Schematic diagram; **(B)** SPS furnace; **(C)** Graphite dies; **(D)** As-sintered specimen with graphite foils; Dimensions of the ground and polished as-sintered specimen: **(E)** Diameter and **(F)** Height; End face liquefaction phenomenon **(G)** 1,070°C and **(H)** 1,090°C.

The purpose of this research is to demonstrate how the various temperatures of sintering influence the microstructure and mechanical properties of SPSed S390 HSS specimens. Moreover, an analysis was performed on the wear behavior and characteristics of dense and porous SPSed S390 HSS specimens as a function of temperature.

2 Materials and methods

S390 PMHSS is primarily utilized for its microstructure of dispersed carbide particles and martensite, which are considered agents the material exceptional hardness, red hardness, and wear resistance. The S390 HSS nitrogen-atomized spherical powders (C: 1.63; Mo: 2.28; W: 10.09; Cr: 4.91; V: 5.12; Co: 8.0; Fe: bal.) was utilized in current study. Dimensional parameters of the powders included 8.44 μm for D_{10}, 32.35 μm for D_{50}, and 117.11 μm for D_{90}, with a flow rate averaged 18.7 s for every 50 g. To obtain a uniform powder mixture, S390 HSS powder and stainless-steel balls were poured into stainless steel jars and mixed for 2 hours at 400 rpm in a planetary ball mill (QM-3SP2, China). The mass ratio of powder to stainless steel balls is 7:1, and the mass ratio of 3 mm stainless steel balls to 5 mm stainless steel balls is 1:1. In order to prevent an increase in oxygen content of powder, sampling and sieving were

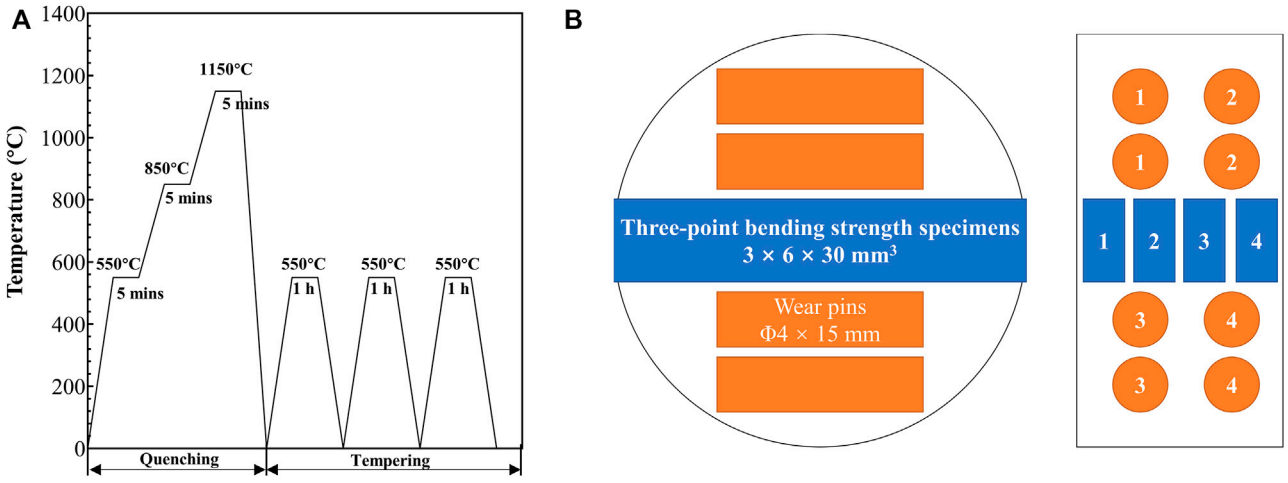

FIGURE 3
Schematic diagram of heat treatment and the sampling position for mechanical tests: **(A)** heat treatment curve **(B)** sampling positions and dimensions.

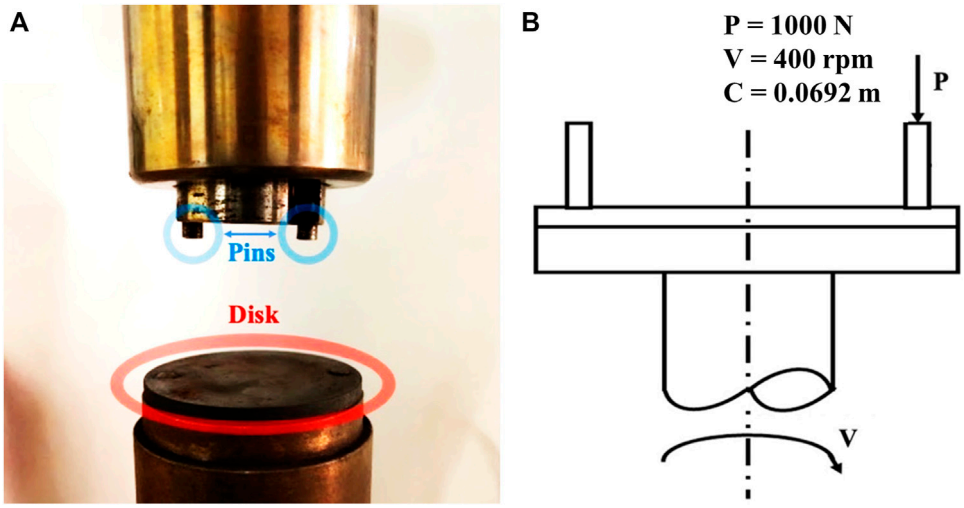

FIGURE 4
The pin-on-disk wear test machine: **(A)** test machine **(B)** schematic diagram.

delayed until the temperature of the jar reached room temperature. The uniform powder mixture was dried to improve the flowability in an air-blowing thermostatic oven (DHG-9035A, China) set to 120°C.

The characterizations of S390 HSS powders were displayed in Figure 1 via scanning electron microscope. The morphology of the powders was captured in Figure 1A, and basically the spherical powders were utilized in this study. The powder corroded by aqua regia is shown in Figure 1B, and the remaining carbides show a three-dimensional distribution of dendrites, which were formed during the rapid cooling of the tiny droplets in gas-atomization process (Ma et al., 2016). Figure 1C exhibited the cross section of the powder under back-scatter electron mode, and the dendrites were distributed evenly in the iron matrix. The states of elements distribution were demonstrated in Figures 1D–I via energy dispersive spectrometer (EDS), the main elements in the matrix were Fe and Co, and the major elements in the carbide dendrites were W, Mo, V and Cr. S390 HSS powders with an irregular morphology, including flaky and hollow powder, were almost removed from the mixture via sieving in order to achieve high density.

2.1 Spark plasma sintering and heat treatment

Powder consolidation was achieved in the Dr. Sinter SPS machine (SPS 1050, Japan), and the schematic diagram and

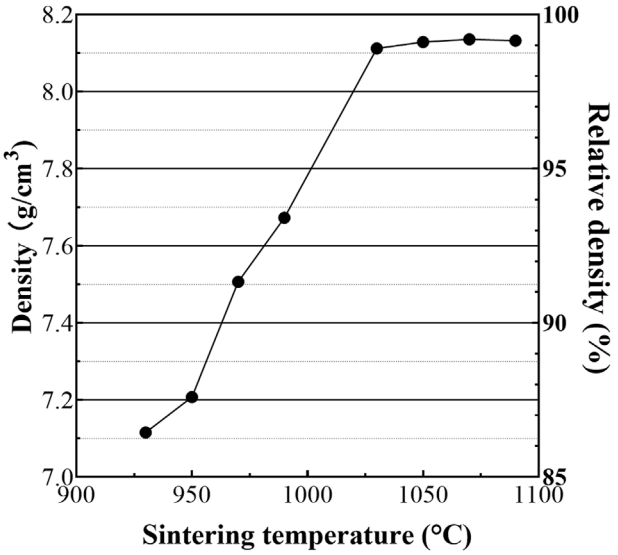

FIGURE 5
Density and relative density of SPSed S390 HSS as a function of sintering temperature.

related macro photos of spark plasma sintering is illustrated in Figures 2A, B. The powders were uniformly mixed before being poured into the graphite die, as shown in Figure 2C, and a layer of graphite foil was inserted between the powders and die to facilitate the process of removing the specimens from the die after sintering. The above specimens (Φ 30 × 18 mm) were prepared at eight different sintering temperatures, each with a uniaxial pressure of 50 MPa and a holding time of 5 min: 930°C, 950°C, 970°C, 990°C, 1,030°C, 1,050°C, 1,070°C, and 1,090°C. The physical pictures of the sintered specimen with different dimensions were shown in Figures 2D–F, an as-sintered specimen with graphite foils should be polished and ground before tests and measurements. With uniaxial pressures beyond 50 MPa, the graphite dies frequently crack during the SPS process, so that no viable specimen was acquired. Since the surface of the as-sintered specimens was not perfectly smooth and was prone to cracking after heat treatment, it was necessary to ground the specimens after removing the graphite foils and before sending them for further heat treatment.

The heat treatment process for HSS primarily consists of a quenching process and triple tempering processes (Becker, 2017). Due to the poor thermal conductivity of HSS, a uniform temperature was unachievable for the specimen, where an uneven temperature easily leads to bending and cracking. Hence the quenching process of HSS is usually a three-stage preheat: low temperature 450°C–650°C, medium temperature 750°C–850°C, and high temperature 1,050°C–1,200°C (Roberts et al., 1998). The carbide in HSS continually dissolves into the matrix at the austenitizing temperature, and the number of carbides in HSS steadily reduces, and the alloying elements diffused into the matrix improve the hardness and wear resistance of the martensitic matrix. It is widely assumed that a high quenching temperature would result in low toughness due to the coarse grain size. Given that the quenching of high-speed steel microstructure contains a high percentage of martensite and residual austenite, tempering should be conducted as soon as possible to ensure microstructure transformation, residual stress reduction, and secondary hardening (Li, 2017). The current heat treatment process was devised with reference to extensive literature and previous experimental results (Peng et al., 2018a; Peng et al., 2018b; Firouzi et al., 2022; Hu et al., 2022). As with the heat treatment depicted in Figure 3A, two-step heating (550°C and 850°C) was employed to guarantee a consistent temperature throughout the austenitizing procedure in a muffle furnace (KJ-A1200-80LWQ, China) with an argon atmosphere. The specimens were then heated to an austenitizing temperature of 1,150°C and oil-quenched to room temperature. An electrical spark incision was utilized to remove the decarburization layer. Finally, the specimens were triple-tempered at 550°C for 1 h, and the cooling procedure was performed at room temperature under air conditioning.

2.2 Characterizations

The densities of the polished as-sintered specimens were measured by weighing them in air and water utilizing the Archimedes' method and converted into a relative density value (the full density was 8.2 g/cm^3). The SPSed S390 HSS specimens were ground with abrasive papers and polished with diamond paste using the traditional metallographic method before optical microscope (OM, Axio Scope 5, German) observation and scanning electron microscope (SEM, Zeiss Gemini 500, German) analysis with secondary electron mode (SE) and back-scatter electron mode (BSE). Before microstructure analysis, some of specimens were necessarily to be etched with $FeCl_3$ solution for 5–10 s. The ImageJ software was utilized for quantitative analysis and statistics on sintered pores (Schneider et al., 2012). The Intermodes mode in the Threshold module extracted pores from OM pictures (certain images were in need of sharpening, especially the images with high sintering temperatures), which were subsequently quantified using the Analyze Particles module. For quantity and feret diameter, the calculations and analyses were repeated in at least four different regions to guarantee the accuracy of the average data.

A digital Rockwell hardness tester (HRS-150D, China) was employed to obtain the room temperature hardness with an applied load of 1471 N and a dwell time of 10 s, and the test should be performed at least five times to obtain accurate average macrohardness values under the same experimental conditions. The red hardness was measured with the specimens tempered at 620°C for 4 h under the same test parameters and experimental conditions. For the three-point bending strength tests, test bars with dimensions of 3 × 6 × 30 mm^3 were cut from the prepared specimens, and at least three test bars were tested for every produced specimen before fracture morphology observations. Figure 3B illustrates the schematic diagram of the sampling position for mechanical tests. In the middle of the specimens, four three-point bending test bars were cut out, as well as four sets of wear pins were cut out from the nearby area. The polished specimens were tested for hardness, and the red hardness was acquired by repeating the tempering test on the tested three-point bending test bars.

An instrument known as a pin-on-disk test machine (MMU-10G, China) was employed to conduct wear tests (MMU-10G, China) as shown in Figure 4A. The two test pins with

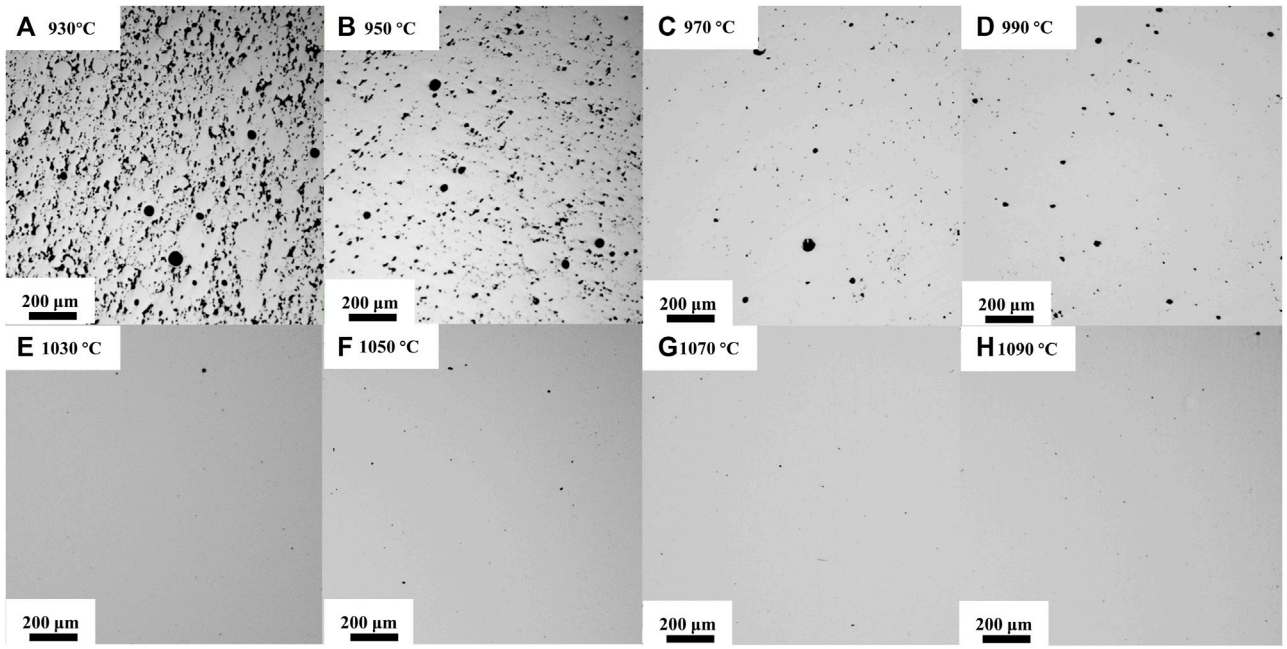

FIGURE 6
Morphology of SPSed S390 HSS specimens at various sintering temperatures: **(A)** 930°C; **(B)** 950°C; **(C)** 970°C; **(D)** 990°C; **(E)** 1,030°C; **(F)** 1,050°C; **(G)** 1,070°C; **(H)** 1,090°C.

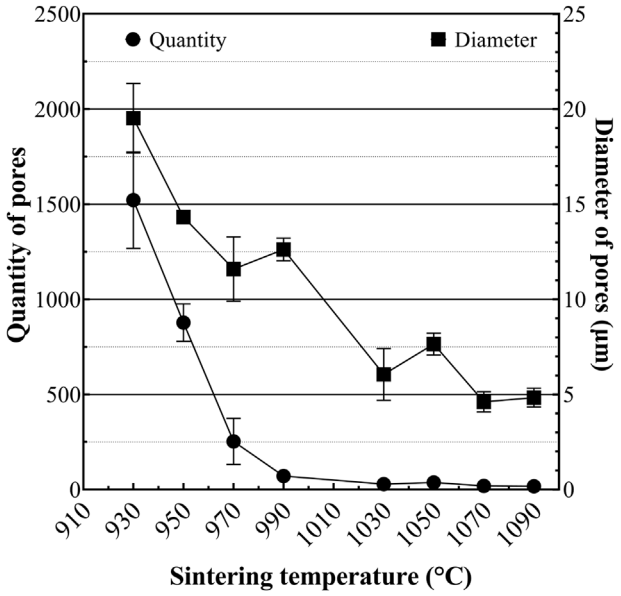

FIGURE 7
Quantity and diameter of pores as a function of sintering temperature.

dimensions of Φ 4 × 15 mm were cut from the materials that had been produced via SPS, and the abrasive disks with a diameter of 43 mm and an average hardness of 68.0 HRC were sliced from the HIPed S390 PMHSS materials. A sliding distance of 553 m (the circumference of the wear track is 0.0692 m in Figure 4B) was accomplished during the wear test that lasted for 20 min and included applying a force of 1000 N to the pins while rotating at a rotating speed of 400 rpm. In order to identify the quantity of mass that was lost due to wear on the pins, the experiment was performed a minimum of three times under identical conditions.

The wear coefficient k of prepared specimens was calculated by the given expression (1):

$$k\left(\frac{m^2}{N}\right) = \frac{\Delta V\left(Abrasive\ volume, m^3\right)}{F\left(Normal\ load, N\right) \times d\left(Sliding\ \ distance, m\right)} \quad (1)$$

The weight loss was measured using an electronic balance with 0.0001 g precision to calculate the abrasive volume ΔV, which was estimable with the following expression (2):

$$\Delta V\left(Abrasive\ volume, m^3\right) = \frac{\Delta m\left(Weight\ loss, g\right)}{\rho\left(density, g/m^3\right)} \quad (2)$$

3 Results and discussion

3.1 Density and microstructure

Figure 5 depicts the correlation between S390 powder HSS density and sintered temperature. As seen in the graph, the sintered density exhibits an overall upward trend with increasing temperature before reaching a steady state. At a sintering temperature of 930°C, the sintered specimen has a density of 7.1 g/cm^3 (86.5%). The density of the specimens increases dramatically with temperature until 1,030°C, reaching a maximum of 8.14 g/cm^3 (99.2%) at 1,070°C. Increasing the

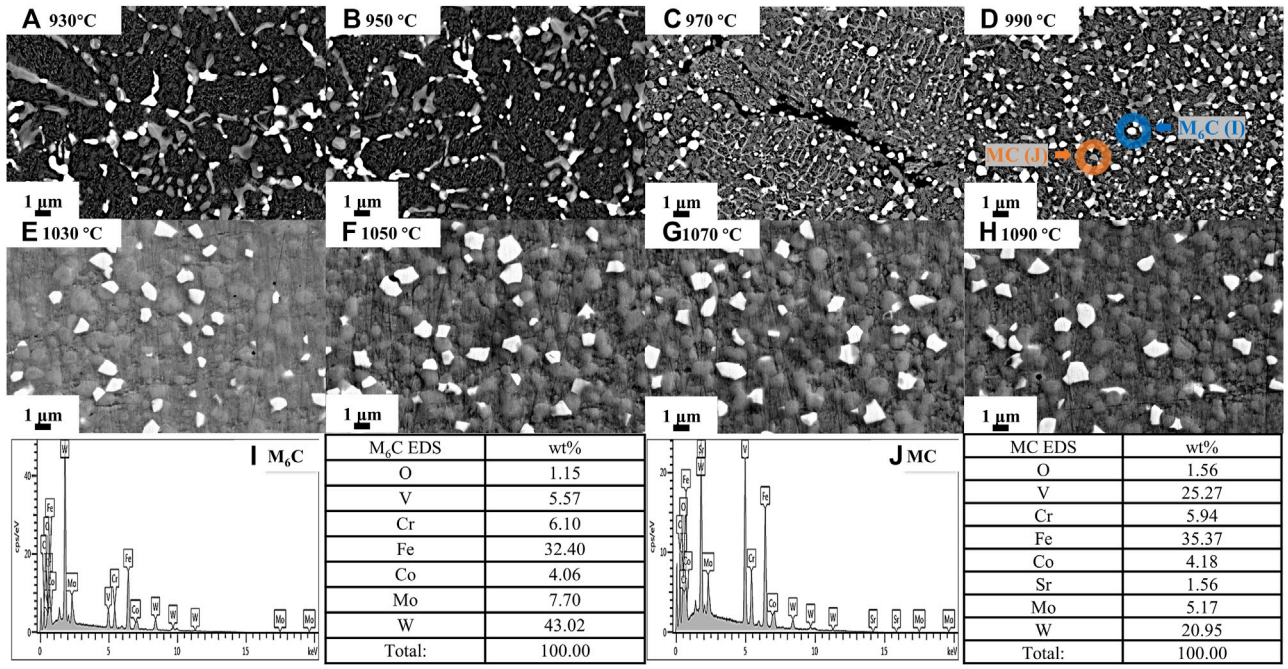

M_6C EDS	wt%
O	1.15
V	5.57
Cr	6.10
Fe	32.40
Co	4.06
Mo	7.70
W	43.02
Total:	100.00

MC EDS	wt%
O	1.56
V	25.27
Cr	5.94
Fe	35.37
Co	4.18
Sr	1.56
Mo	5.17
W	20.95
Total:	100.00

FIGURE 8
Microstructure of S390 HSS specimens at various sintering temperatures: BSE-SEM: **(A)** 930°C, **(B)** 950°C, **(C)** 970°C, and **(D)** 990°C; SE-SEM: **(E)** 1,030°C, **(F)** 1,050°C, **(G)** 1,070°C, and **(H)** 1,090°C; EDS spectrums and chemical compositions: **(I)** M_6C, **(J)** MC.

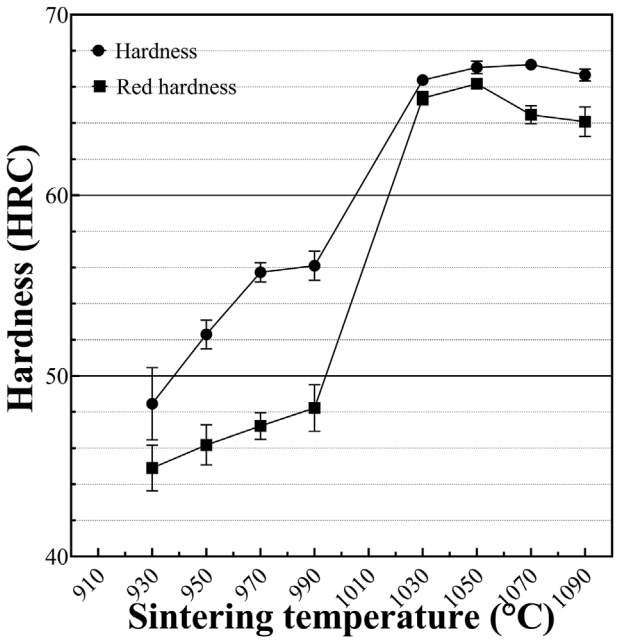

FIGURE 9
Hardness and red hardness of SPSed S390 HSS as a function of sintering temperature.

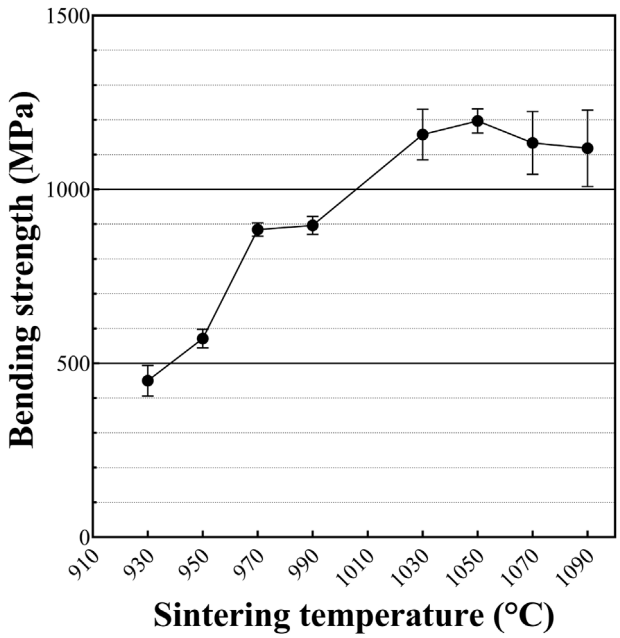

FIGURE 10
Three-point bending strength of SPSed S390 HSS as a function of sintering temperature.

sintering temperature further has no major effect on the density of the specimens. During the sintering process, the increase in temperature promotes atomic vibrations and facilitates diffusion behavior, beginning with the formation of adhesive contact points between the powders, then gradually forming sintering necks with increasing time, and finally growing and bridging the sintering necks

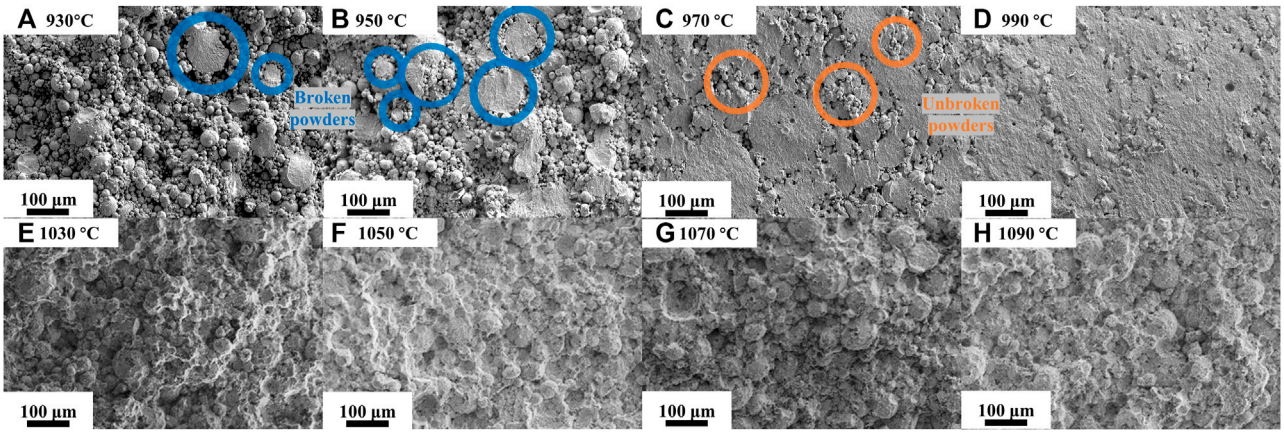

FIGURE 11
Fracture morphologies of SPSed S390 HSS specimens after three-point bending strength tests at various sintering temperatures: **(A)** 930°C, **(B)** 950°C, **(C)** 970°C, **(D)** 990°C, **(E)** 1030°C, **(F)** 1050°C, **(G)** 1070°C, **(H)** 1090°C.

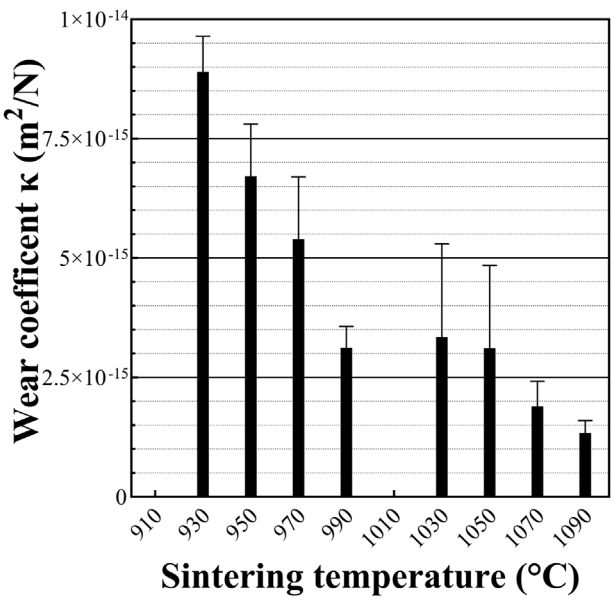

FIGURE 12
Wear coefficients of SPSed S390 HSS as a function of sintering temperature.

to spheroidize the pores. In addition, as shown in Figures 2G, H, for the discharge plasma sintering process, the high sintering temperature causes the powder material to melt and be extruded onto the end face of the specimen, thereby reducing the effect of the applied pressure on the internal powder and reducing the density of the sintered specimen to 8.13 g/cm^3 (99.1%) at 1,090°C.

Micrographs taken using an OM and a SEM, respectively, exhibiting sintering at various temperatures are shown in Figures 6, 8. It is clear from examining Figure 6A that the pores in the sintered specimen at 930°C take up a considerable amount of space. Even in the sintered specimen shown in Figure 6H at 1,090°C, a tiny number of pores were detected, suggesting the impossibility of a total eradication, as the size and area of the pores in the specimen shown in Figures 6B–G progressively diminish and gradually spheroidize as the sintering temperature rises. Since the analysis and statistics of sintering pores have been conducted on OM images via ImageJ software, Figure 7 shows that as the sintering temperature raised, both the quantity of pores and their diameter decreased significantly, from an average of 1,521 pores per field of view down to 17 pores and from 19.5 μm down to 4.8 μm, respectively. Furthermore, a simulation study on spark plasma sintering reveals that the temperature field of the powder in sintering was not uniform, and the circular pores in the hollow powder that were easily seen in specimens sintered at low temperatures were also seen in specimens sintered at high temperatures, but their size was much smaller and not completely eliminated, which might be related to the local soft melting and viscosity reduction of the powders at high temperatures (Liu et al., 2006; Zhang et al., 2022; Yu et al., 2023). The microstructure of S390 powdered HSS in SEM backscattered electron mode at various sintering temperatures is shown in Figure 8. All of the sintered specimens showed granular carbides that get larger with higher temperatures. The EDS spectra and chemical composition of the 990°C sintered specimens revealed that the white carbides were mostly M_6C with a high intensity of W and the dark gray ones were MC with a high intensity of V, the similar microstructure analyses have been reported (Godec et al., 2010; Leskovšek and Podgornik, 2012; Jin et al., 2020). Thus, increasing the sintering temperature has a substantial impact on pore removal. Sintering necks get larger as temperatures rise because more elements diffuse into the material, yet tiny pores are eliminated as grain sizes grow. Sintering raises the temperature, causing the two carbides to precipitate either along the carbide dendrites or directly in the iron matrix, where they eventually form two granular carbides that are widely dispersed over the matrix.

3.2 Mechanical properties

The hardness of HSS is the most crucial property, since higher hardness is typically associated with better wear resistance. Figure 9 shows the effect of sintering temperatures on hardness and red hardness. Overall, the hardness variation tends to grow fast below

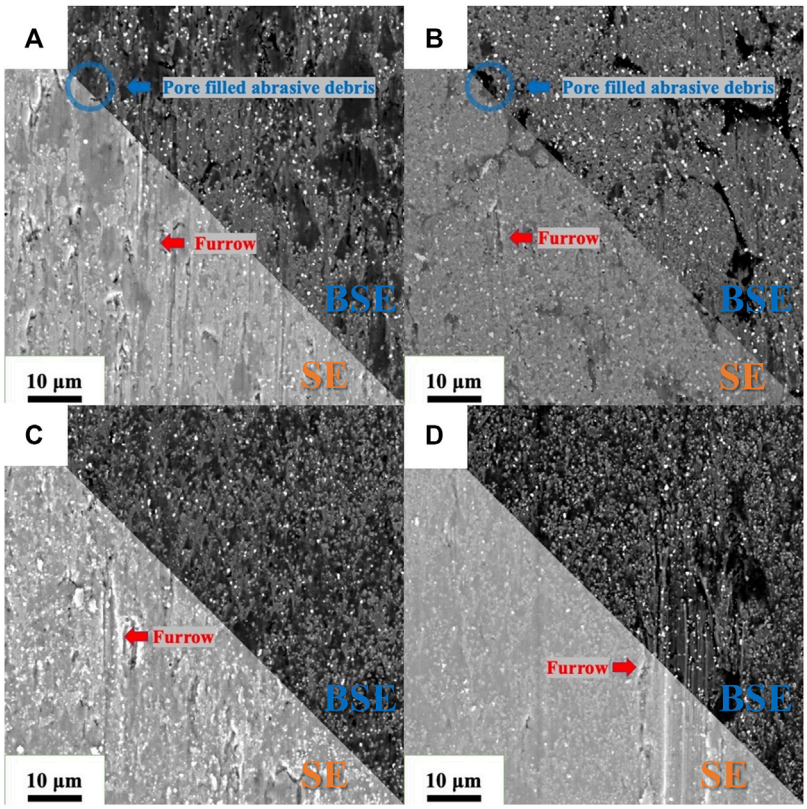

FIGURE 13
Worn surfaces of SPSed S390 HSS at various sintering temperatures: **(A)** 930°C; **(B)** 950°C; **(C)** 970°C; **(D)** 990°C.

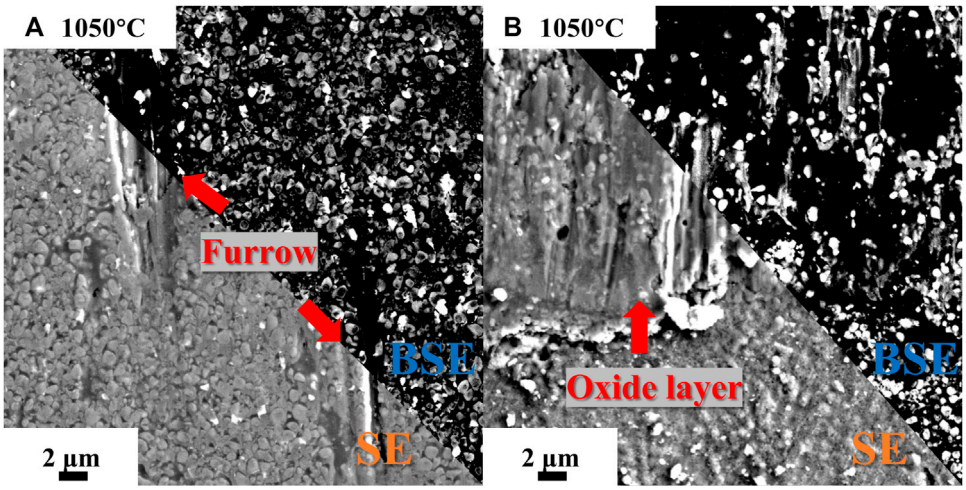

FIGURE 14
Worn surfaces of S390 HSS at 1,050°C: **(A)** Furrows; **(B)** Oxide layer.

1,030°C and stabilizes beyond this temperature. The specimen sintered at 930°C measured the softest (48.46 HRC), and hardness rose with increasing sintering temperature, reaching 56.1 HRC in a specimen prepared at 990°C. Nonetheless, this was still much lower than predicted. Sintered specimens entered a stable hardness zone at temperatures over 1,030°C, with all specimens

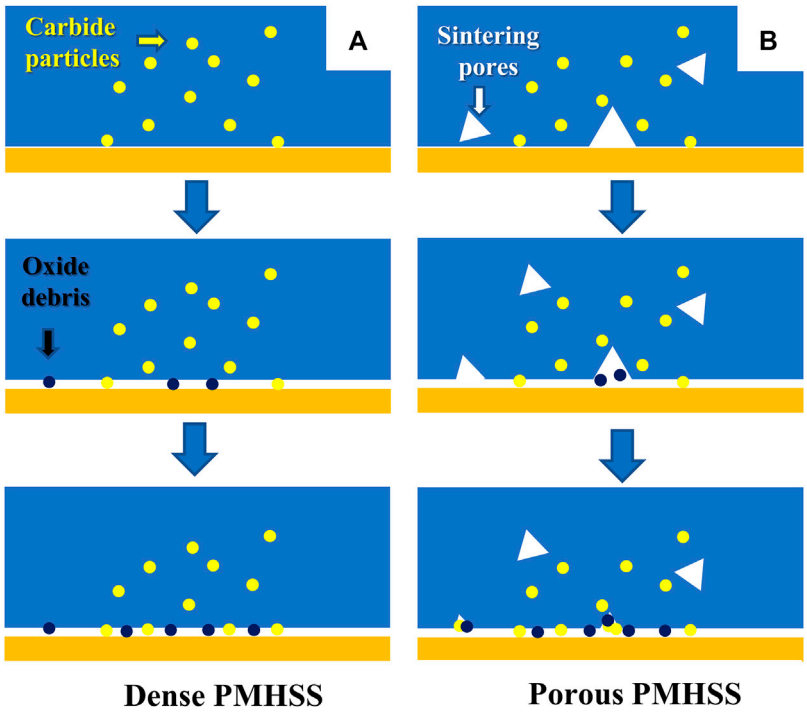

FIGURE 15
Wear mechanism of PMHSS: **(A)** Dense PMHSS; **(B)** Porous PMHSS.

exhibiting a hardness greater than 66 HRC and the specimen sintered at 1,070°C having the maximum hardness of 67.2 HRC. Excellent hardness was demonstrated by the specimens produced at this range of sintering temperatures, and the strengthening mechanism of dense PMHSS consists of two main aspects: on the one hand, the solid solution strengthening mechanism stems from the austenite to martensite transformation of the iron matrix, and on the other hand, the dispersion strengthening mechanism stems from two fine and uniformly distributed high-hardness carbides (MC and M_6C) (Peng et al., 2018a; Peng et al., 2018b; Mao et al., 2021; Cui et al., 2022). Hardness refers to the ability of a material to locally resist the pressure of a hard object into its surface. For specimens with sintering temperatures below 990°C, the relative density values of these specimens were less than 94%, and the main microstructural modification was the simultaneous decrease in the quantity and dimensions of the pores, which might be the chief explanation for their increased hardness. Significant changes in the microstructure also occurred at this stage, such as a shift from rod-like carbides to particulate carbides, that might be primarily responsible for the increase in hardness compared to the specimens sintered at temperatures greater than 1,030°C. For the specimens sintered at temperatures higher than 1,030°C, the relative density values of these specimens were relatively close, and the microstructures all presented a homogenous distribution of carbides of similar size on the iron matrix, hence their hardness values were in a stable zone above 66 HRC. These hardness values of the specimens after the red-hardness test followed a generally similar trend regardless of their sintering temperatures, with the exception of a little drop (2.5 HRC) in hardness for the specimens sintered at 1,070°C and 1,090°C, and the highest hardness value was measured in a specimen sintered at 1,050°C. Carbide formation is related to the hardening of high-speed steel after using it, and the absence of elements that form carbides from the iron matrix weakens the strengthening effect of the matrix on the steel due to solid solution. This phenomenon has been thoroughly explored in several scholarly works. The hardness and red-hardness test results demonstrated that the specimen sintered at 1,050°C had a better performance in service.

Inadequate toughness, for example, might induce chipping in cutting tools, hence, toughness is an essential HSS attribute that greatly affects the quality and lifespan of cutting tools. As shown in Figure 10, a higher sintering temperature resulted in greater three-point bending strength. The tendency for three-point bending strength was divided into three main stages. For the first stage, the three-point bending strengths of specimens sintered at 930°C and 950°C were 450 and 570 MPa, respectively. Specimens sintered at 970°C and 990°C exhibited a three-point bending strength of 884 and 896 MPa, respectively, nearly twice that of the first stage. The final stage specimens all had strengths greater than 1,100 MPa, with the specimen sintered at 1,150°C achieving the highest (1,196 MPa). Thereafter, as the sintering temperature rose, the three-point bending strength steadily declined. Referring to the results in Figure 8, the carbide characteristics might be one of the factors affecting the three-point bending strength. In the first stage, the carbides appeared as a short rod, while in the second stage, their carbides morphology transformed into a particle shape with a diameter of less than 1 μm, and in the last stage, the carbides completely transformed into a particle shape with a size slightly

larger than 1 μm. The higher sintering temperature could cause the growth of carbides, which might deteriorate the three-point bending strength in the last stage. A study of SPSed M3:2 HSS reckoned that excessive growth of grains due to high sintering temperatures might be attributed to declination of properties (Zhou et al., 2014). As has been investigated by numerous researchers on impact toughness and bending strength, coarse carbides or an uneven distribution of carbides is a frequent cause of inferior toughness in HSS. The toughness of HSS is affected by the quantity, variety, shape, and distribution of carbides, all of which are typically influenced by the forming and heat treatment procedures (Lu et al., 2016; Lyu et al., 2021; Firouzi et al., 2022).

The fracture surfaces of the test bars at multiple sintering temperatures were studied using SEM with SE mode to further investigate the factors affecting the three-point bending strength, as shown in Figure 11. Slight amounts of large powders (above 50 μm, Figures 11A, B) fractured during the first stage of the test bars, whereas substantial quantities of tiny particle powders (below 50 μm, Figures 11C, D) that retained their spherical shape could be seen at the fracture surfaces in Figures 11A, B. At the second stage, shown in Figures 11C, D, the test bars had flatter fracture surfaces, and the pores were smaller and less noticeable than in the first. At this stage, all but a tiny quantity of the fine powders (below 20 μm) had contributed to the three-point bending strength tests. Figures 11G, H showed fractures at the prior powder boundary as well as quasi-cleavage fractures, defined by tiny facets and tear ridges (Cho et al., 2021; Yuan et al., 2023), on the fracture surfaces of test bars at this stage in Figures 11E–H. In the first stage, the sintering temperature was lower, and due to the large surface area of the larger powders, their probability and number of forming the sintering neck were much higher than that of the smaller powders. Furthermore, a simulated investigation of the sintering neck between two metal powders in the SPS process demonstrated that the sintering neck of large powders was wider than that of tiny powders (Liu et al., 2006). Thus, the larger powders would preferentially fracture and contribute to the three-point bending strength. In the second stage, as the sintering temperature increased, the smaller powders also formed sintering necks with other powders. The formation and growth of the sintering necks reduced the size and number of pores, and although the carbides in the microstructure of the specimens at the second stage transformed into particles, the flat fracture surface indicated that the strength of the sintering necks was higher than that of the powder interiors. In the last stage, the fracture surface exhibited similar characteristics to the other HSS, but fractures along the original powder boundary were seen in the two specimens with higher sintering temperatures, which might be related to the excessive sintering temperatures in the SPS process resulting in incomplete loading of the end face because of high-temperature-induced liquefied powders.

3.3 Wear property and mechanism

The wear coefficient, defined as the volume of wear induced by sliding a unit distance under a unit force, could be utilized to quantify the wear resistance of a material. As shown in Figure 12, the wear coefficient decreased as the temperature rose, indicating that the wear resistance of the specimens improved. The specimen with the weakest wear resistance was sintered at 930°C with an average wear coefficient of 8.89×10^{-15} m^2/N, while the specimen with the strongest wear resistance was sintered at 1,090°C with an average wear coefficient of 1.33×10^{-15} m^2/N. Notably, the wear coefficients of the specimens sintered at 990, 1,030, and 1,050°C were almost identical (3.12×10^{-15}, 3.34×10^{-15}, and 3.11×10^{-15} m^2/N). The improvement in wear coefficient as a function of sintering temperatures could be attributed to the microstructure evolution, which was actually characterized by the removal of pores and the growth of carbides. Recent research results on the wear coefficient of PMHSS were basically similar to the present study. M3:2 PMHSS were prepared with multiple carbide reinforcement schemes, and the strongest average wear coefficient (about 1.15×10^{-14} m^2/N) was measured in a specimen sintered at 1,190°C with 10 vol.% of TaC and NbC (Gordo et al., 2000). The high-vanadium HSSs were prepared, and the highest wear coefficient of specimens sintered at 1,250°C was 4.31×10^{-15} m^2/N (Wan et al., 2019). The 10.8 wt.% Cr addition could enhance the wear coefficient of a high-boron HSS to around 4.82×10^{-14} m^2/N (Guo et al., 2022).

More details were revealed by observing the worn surfaces of the pins via SEM, and the results are exhibited in Figures 13, 14. Referring to Figures 6, 8, besides the carbides and sintered pores uniformly distributed on the iron matrix, furrows with a width of around 2 μm in SE-SEM images and pores filled with oxide debris and carbides in BSE-SEM image morphology were also noted in Figures 13A–D for specimens sintered at 930°C–990°C. And the worn surfaces of specimens sintered at 1,030°C–1,090°C were featured with about 3 μm wide furrows and a small amount of oxide layers. The wear mechanism of the behaviors were illustrated in Figure 15, numerous scientific reports had revealed that the wear mechanism of dense HSS contained abrasive wear characterized by furrows (Wei et al., 2005) and oxidation wear characterized by debris and oxide layers (Guo et al., 2022), and the detached debris and carbides accelerated the transition between two-body and three body abrasive wear (Trezona et al., 1999), which was also confirmed in this study and depicted in Figure 15A. As for the wear coefficients of the specimens sintered at 990, 1,030, and 1,050°C were almost identical (3.12×10^{-15}, 3.34×10^{-15}, and 3.11×10^{-15} m^2/N), this phenomenon might be explained by two behaviors. The first behavior could be low mass loss because of the debris and carbides trapped inside the sintering pores (Salahinejad et al., 2010), while the second behavior might be a high quantity of carbides on the worn surface due to the trapped hard carbides in Figure 15B. For porous test pins, the trapped carbides not only increased the quantity of carbides on the worn surface and thus improved the wear resistance of the surface for a short period of time but also reduced the effect of three-body abrasive wear. For the wear mechanism of porous materials, trapped debris might reduce the mass that should be lost; however, a material reinforced with hard particles, which have a lower dimension than pores, could enhance the worn surface by the process of hard particle detachment and re-servicing.

4 Conclusion

In this study, the effects of sintering temperatures on the microstructure and mechanical properties of S390 PMHSS were

considered. The outcome of this research could be summarized as follows:

(1) The density and relative density were improved by the elevated sintering temperature, and the sintering temperature had an influence on the microstructure, especially in the morphology and dimension of pores and carbides. The analysis and statistics of pores showed that the quantity of pores and their diameter decreased significantly. Besides, the diminish of the circular pores in the hollow powder was related to spark plasma sintering process and the local soft melting.
(2) Mechanical properties such as hardness and three-point bending strength improved significantly as the sintering temperature rose. The reduction of pores contributes to the hardness increase in the low sintering temperature stage, while the solid solution strengthening mechanism in martensitic matrix and the dispersion strengthening mechanism from fine high-hardness carbides serve as reasons for the elevated hardness in the high sintering temperature stage; the specimen with the best comprehensive mechanical properties (67.1 HRC and 1,196.67 MPa) was prepared at 1,050°C.
(3) The wear coefficients exhibited a downward tendency with increasing sintering temperatures, and the observation results of worn surfaces of test pins confirmed that abrasive wear and oxidation wear dominated the wear experiments. Besides, the wear mechanism of dense and porous SPS HSS was illustrated and analyzed.

Data availability statement

The original contributions presented in the study are included in the article/supplementary material, further inquiries can be directed to the corresponding authors.

Author contributions

Conceptualization, QH and MW; methodology, QH; validation, QH; investigation, QH; resources, YC; data curation, QH; writing—original draft preparation, QH; writing—review and editing, DZ and ZS; supervision, MW; project administration, MW; funding acquisition, MW. All authors contributed to the article and approved the submitted version.

Funding

The authors acknowledge funding support from the National Natural Science Foundation of China, under Grant Number "51975240".

Conflict of interest

Authors QH, MW, YC, and ZS were employed by China Academy of Machinery Science and Technology Group Co., Ltd. Authors QH, MW, YC, and DZ were employed by Beijing National Innovation Institute of Lightweight Co., Ltd. Authors QH, MW, and DZ were employed by China Machinery Institute of Advanced Materials Co., Ltd.

Publisher's note

References

Asgharzadeh, H., and Simchi, A. (2005). Effect of sintering atmosphere and carbon content on the densification and microstructure of laser-sintered M2 high-speed steel powder. *Mat. Sci. Eng. A* 403 (1-2), 290–298. doi:10.1016/j.msea.2005.05.017

Becker, O. M. (2017). *High-speed steel - the development, nature, treatment, and use of high-speed steels, together with some suggestions as to the problems involved in their use*. New York, Ny, USA: Read Books Limited.

Benito, S., Boes, J., Matsuo, M., Weber, S., and Theisen, W. (2021). Uncovering process-structure relationships associated to the hot isostatic pressing of the high-speed steel PMHS 3-3-4 through novel microstructural characterization methods. *Mat. Des.* 208, 109925–109929. doi:10.1016/j.matdes.2021.109925

Cho, L., Bradley, P. E., Lauria, D. S., Martin, M. L., Connolly, M. J., Benzing, J. T., et al. (2021). Characteristics and mechanisms of hydrogen-induced quasi-cleavage fracture of lath martensitic steel. *Acta Mater* 206, 116635–116643. doi:10.1016/j.actamat.2021.116635

Cui, K. K., Mao, H. B., Zhang, Y. Y., Wang, J., Wang, H., Tan, T. B., et al. (2022). Microstructure, mechanical properties, and reinforcement mechanism of carbide toughened ZrC-based ultra-high temperature ceramics: A review. *Compos. Interfaces* 29 (7), 729–748. doi:10.1080/09276440.2021.2012409

Firouzi, A., Yazdani, S., Tavangar, R., Shakerifard, B., and Mohammad, F. K. (2022). Austempering of PM HSS ASP2030 for improved fracture toughness. *Metall. Res. Technol.* 119 (2), 211–220. doi:10.1051/metal/2022025

Furuya, K., Jitsukawa, S., and Saito, T. (2022). Application of the sinter-HIP method to manufacture Cr-Mo-W-V-Co high-speed steel via powder metallurgy. *Mater. (Basel)* 15 (6), 221–228. doi:10.3390/ma15062300

Godec, M., Batič, B. Š., Mandrino, D., Nagode, A., Leskovšek, V., Škapin, S. D., et al. (2010). Characterization of the carbides and the martensite phase in powder-metallurgy high-speed steel. *Mat. Charact.* 61 (4), 452–458. doi:10.1016/j.matchar.2010.02.003

Gordo, E., Velasco, F., Antón, N., and Torralba, J. M. (2000). Wear mechanisms in high speed steel reinforced with (NbC)p and (TaC)p MMCs. *Wear* 239 (2), 251–259. doi:10.1016/s0043-1648(00)00329-x

Guo, P., Ma, S., Jiao, M., Lv, P., Xing, J., Xu, L., et al. (2022). Effect of chromium on microstructure and oxidation wear behavior of high-boron high-speed steel at elevated temperatures. *Mater. (Basel)* 15 (2), 441–447. doi:10.3390/ma15020557

Hasan, M., Islam, M. A., Huang, Z. Y., Zhao, J. W., and Jiang, Z. Y. (2023). Influence of sintering time on diffusion bonding of WC-10Co and AISI4340 by spark plasma sintering. *Mat. Sci. Technol.* 39 (6), 683–693. doi:10.1080/02670836.2022.2132732

Herranz, G., Matula, G., and Romero, A. (2017). Effects of chromium carbide on the microstructures and wear resistance of high speed steel obtained by powder injection moulding route. *Powder Metall.* 60 (2), 120–130. doi:10.1080/00325899.2017.1288778

Hu, Q., Wang, M., Chen, Y., Liu, H., and Si, Z. (2022). The effect of MC-type carbides on the microstructure and wear behavior of S390 high-speed steel produced via spark plasma sintering. *Metals* 12 (12), 2168–2180. doi:10.3390/met12122168

Jin, J., Gao, R., Peng, H., Guo, H., Gong, S., and Chen, B. (2020). Rapid solidification microstructure and carbide precipitation behavior in electron beam melted high-speed steel. *Metall. Mat. Trans. A* 51 (5), 2411–2429. doi:10.1007/s11661-020-05661-z

Leskovšek, V., and Podgornik, B. (2012). Vacuum heat treatment, deep cryogenic treatment and simultaneous pulse plasma nitriding and tempering of P/M S390MC steel. *Mat. Sci. Eng. A* 531, 119–129. doi:10.1016/j.msea.2011.10.044

Li, H. (2017). *Technology and practice of heat treatment of tool materials*. Beijing, China: China Machine Press.

Li, Y., Wang, Y., Niu, J., Liu, S., Lin, Y., Liu, N., et al. (2023). Microstructure and mechanical properties of M2 high speed steel produced by electron beam melting. *Mat. Sci. Eng. A* 862, 13–19. doi:10.1016/j.msea.2022.144327

Liu, X., Song, X., and Zhang, J. (2006). Temperature distribution simulation and neck evolution of powder particles during spark plasma sintering. *Acta Metall. Sin.* 42 (7), 757–762. doi:10.3321/j.issn:0412-1961.2006.07.015

Lu, L., Hou, L. G., Zhang, J. X., Wang, H. B., Cui, H., Huang, J. F., et al. (2016). Improved the microstructures and properties of M3:2 high-speed steel by spray forming and niobium alloying. *Mat. Charact.* 117, 1–8. doi:10.1016/j.matchar.2016.04.010

Lyu, C., Zhou, J., Zhang, X., Yao, Y., and Zhang, Y. (2021). Effect of heat treatment on microstructure and impact toughness of a Tungsten-Molybdenum powder metallurgical high-speed steel. *Mat. Sci. Eng. A* 815, 141268–141276. doi:10.1016/j.msea.2021.141268

Ma, J., Wang, B., Yang, Z., Wu, G., Zhang, J., and Zhao, S. (2016). Microstructure simulation of rapidly solidified ASP30 high-speed steel particles by gas atomization. *Int. J. Min. Metall. Mat.* 23 (3), 294–302. doi:10.1007/s12613-016-1238-8

Madej, M., Leszczynska-Madej, B., and Garbiec, D. (2022). Effect of sintering temperature and iron addition on properties and microstructure of high speed steel based materials produced by spark plasma sintering method. *Mater. (Basel)* 15 (21), 12–19. doi:10.3390/ma15217607

Mao, H. B., Shen, F. Q., Zhang, Y. Y., Wang, J., Cui, K. K., Wang, H., et al. (2021). Microstructure and mechanical properties of carbide reinforced TiC-based ultra-high temperature ceramics: A review. *Coatings* 11 (12), 18–42. doi:10.3390/coatings11121444

Matteazzi, P., and Wolf, F. (1998). Mechanomaking of high speed steel AISI M2 powders fabrication. *Mat. Sci. Eng. A* 246 (1-2), 235–243. doi:10.1016/s0921-5093(97)00748-x

Mukund, B. N., and Hausnerova, B. (2020). Variation in particle size fraction to optimize metal injection molding of water atomized 17–4PH stainless steel feedstocks. *Powder Technol.* 368, 130–136. doi:10.1016/j.powtec.2020.04.058

Oke, S. R., Ige, O. O., Falodun, O. E., Obadele, B. A., Shongwe, M. B., and Olubambi, P. A. (2018). Optimization of process parameters for spark plasma sintering of nano structured SAF 2205 composite. *J. Mat. Res. Technol.* 7 (2), 126–134. doi:10.1016/j.jmrt.2017.03.004

Park, D. W., Do, K. R., Kwon, Y. S., Cho, K. K., Lim, S. G., and Ahn, I. S. (2011). Fabrication and properties of T42 sintered part using spark plasma sintering. *Rev. Adv. Mat. Sci.* 28 (1), 103–106.

Peng, H., Hu, L., Li, L., Zhang, L., and Zhang, X. (2018a). Evolution of the microstructure and mechanical properties of powder metallurgical high-speed steel S390 after heat treatment. *J. Alloys Compd.* 740, 766–773. doi:10.1016/j.jallcom.2017.12.264

Peng, H., Hu, L., Zhang, X., Wei, X., Li, L., and Zhou, J. (2018b). Microstructural evolution, behavior of precipitates, and mechanical properties of powder metallurgical high-speed steel S390 during tempering. *Metall. Mat. Trans. A* 50 (2), 874–883. doi:10.1007/s11661-018-5040-2

Roberts, G. A., Kennedy, R., and Krauss, G. (1998). *Tool steels*. 5th. New York, NY, USA: ASM International.

Romero, A., Rodríguez, G. P., and Barea, R. (2020). Sinter-hardening of chromium PM steels with concentrated solar energy. *J. Mat. Process. Technol.* 280, 15–27. doi:10.1016/j.jmatprotec.2020.116616

Shashanka, R., and Chaira, D. (2016). Effect of sintering temperature and atmosphere on nonlubricated sliding wear of nano-yttria-dispersed and yttria-free duplex and ferritic stainless steel fabricated by powder metallurgy. *Tribol. Trans.* 60 (2), 324–336. doi:10.1080/10402004.2016.1168897

Salahinejad, E., Amini, R., Marasi, M., and Hadianfard, M. J. (2010). Microstructure and wear behavior of a porous nanocrystalline nickel-free austenitic stainless steel developed by powder metallurgy. *Mat. Des.* 31 (4), 2259–2263. doi:10.1016/j.matdes.2009.10.008

Schneider, C. A., Rasband, W. S., and Eliceiri, K. W. (2012). NIH image to ImageJ: 25 years of image analysis. *Nat. Methods* 9 (7), 671–675. doi:10.1038/nmeth.2089

Shen, B., Du, B., Wang, M., Xiao, N., Xu, Y., and Hao, S. (2019). Comparison on microstructure and properties of stainless steel layer formed by extreme high-speed and conventional laser melting deposition. *Front. Mat.* 6, 55–63. doi:10.3389/fmats.2019.00248

Shen, W., Yu, L., Liu, H., He, Y., Zhou, Z., and Zhang, Q. (2020). Diffusion welding of powder metallurgy high speed steel by spark plasma sintering. *J. Mat. Process. Technol.* 275, 116383–116398. doi:10.1016/j.jmatprotec.2019.116383

Trezona, R. I., Allsopp, D. N., and Hutchings, I. M. (1999). Transitions between two-body and three-body abrasive wear: Influence of test conditions in the microscale abrasive wear test. *Wear* 225-229, 205–214. doi:10.1016/s0043-1648(98)00358-5

Wan, S., Li, H., Tieu, K., Xue, Q., and Zhu, H. (2019). Mechanical and tribological assessments of high-vanadium high-speed steel by the conventional powder metallurgy process. *Int. J. Adv. Manuf. Technol.* 103 (1-4), 943–955. doi:10.1007/s00170-019-03547-y

Wang, H., Feng, S., Gong, X., Guo, Y., Xiang, P., Fang, Y., et al. (2021). Dynamic performance detection of CFRP composite pipes based on quasi-distributed optical fiber sensing techniques. *Front. Mat.* 8, 43–56. doi:10.3389/fmats.2021.683374

Wang, Y., Chu, S., Mao, B., Xing, H., Zhang, J., and Sun, B. (2022). Microstructure, residual stress, and mechanical property evolution of a spray-formed vanadium-modified high-speed steel processed by post-heat treatment. *J. Mat. Res. Technol.* 18, 1521–1533. doi:10.1016/j.jmrt.2022.03.053

Wei, S., Zhu, J., and Xu, L. (2005). Research on wear resistance of high speed steel with high vanadium content. *Mat. Sci. Eng. A* 404 (1-2), 138–145. doi:10.1016/j.msea.2005.05.062

Xiang, P., Lin, Y., Huang, W., Ding, F., Ye, B., and Deng, Z. (2020). Investigation on shear capacity of joints between steel reinforced concrete special-shaped column and reinforced concrete beam. *Front. Mat.* 7, 77–84. doi:10.3389/fmats.2020.588296

Xu, G., Huang, P., Wei, Z., Feng, Z., and Zu, G. (2022). Microstructural variations and mechanical properties of deep cryogenic treated AISI M35 high-speed steel tempered at various temperatures. *J. Mat. Res. Technol.* 17, 3371–3383. doi:10.1016/j.jmrt.2022.02.083

Yamanoglu, R., Bradbury, W., Olevsky, E. A., and German, R. M. (2013). Sintering and microstructure characteristics of 42CrMo4 steel processed by spark plasma sintering. *Mater. Mat. Int.* 19 (5), 1029–1034. doi:10.1007/s12540-013-5015-1

Yan, J., Wang, J., Chen, H., and Xiang, P. (2022). High temperature exposure assessment of graphene oxide reinforced cement. *Front. Mat.* 9, 15–33. doi:10.3389/fmats.2022.786260

Yang, B., Xiong, X., Liu, R., Chen, J., Yang, J., and Luan, H. (2021). Effect of yttrium hydride addition on microstructure and properties of powder metallurgy CM2 high speed steel. *J. Mat. Res. Technol.* 14, 1275–1283. doi:10.1016/j.jmrt.2021.07.056

Yu, L. H., Zhang, Y. Y., Mao, H. B., Cui, K. K., and Liu, H. L. (2023). Structure evolution, properties and synthesis mechanism of ultra-lightweight eco-friendly ceramics prepared from kaolin clay and sewage sludge. *J. Environ. Chem. Eng.* 11 (1), 14–15. doi:10.1016/j.jece.2022.109061

Yuan, Z., He, Y., Xie, F., and Kang, X. (2023). Effects of Ti(C,N) additions on the microstructure and properties of the carbon-free high speed steel reinforced by intermetallic compounds. *Intermetallics* 152, 11–16. doi:10.1016/j.intermet.2022.107767

Zeng, H., Wu, H., Zhou, C., Liu, Y., and Liu, B. (2019). Effects of sintering temperature on microstructure and properties of high speed steel particles reinforced titanium matrix composites. *Mat. Sci. Eng. Powder. Metall.* 24 (1), 68–73.

Zhang, X., Xia, Q., Ye, B., Yan, W., Deng, Z., and Xiang, P. (2021). Seismic performances of SRC special-shaped columns and RC beam joints under double-direction low-cyclic reversed loading. *Front. Mat.* 8, 23–41. doi:10.3389/fmats.2021.761376

Zhang, Y. Y., Yu, L. H., Wang, J., Mao, H. B., and Cui, K. K. (2022). Microstructure and mechanical properties of high strength porous ceramics with high sewage sludge content. *J. Clean. Prod.* 380, 13–14. doi:10.1016/j.jclepro.2022.135084

Zhang, Z., Chen, Y., Zhang, Y., Gao, K., Zuo, L., Qi, Y., et al. (2017). Tribology characteristics of ex-situ and *in-situ* tungsten carbide particles reinforced iron matrix composites produced by spark plasma sintering. *J. Alloys Compd.* 704, 260–268. doi:10.1016/j.jallcom.2017.02.003

Zhou, R., Diao, X. G., Chen, J., Du, X. N., Yuan, G. D., and Sun, G. F. (2014). "Effect of spark plasma sintering on the microstructure evolution and properties of m3:2 high-speed steel," in *Mater. Sci. Forum*. Shandong, China: International Union of Materials Research Societies).